Materials Advances

ROYAL SOCIETY OF CHEMISTRY

PAPER

View Article Online
View Journal | View Issue

Cite this: *Mater. Adv.*, 2026, 7, 5693

Synthesis of a novel visible light-driven and magnetically separable photocatalyst based on a $BiFeO_3$–$YFeO_3$ type II heterojunction

Sofia M. Tikhanova,[a] Mikhail P. Volkov,[b] Ivan V. Buryanenko,[c]
Valentin G. Semenov,[cd] Zhandos Orazov,[e] Valentin Romanovski, *[f]
Vadim I. Popkov[a] and Natalia A. Lomanova*[g]

Nanocomposites based on the $BiFeO_3$–$YFeO_3$ system with different phase ratios have been synthesized *via* the solution combustion route. The nominal compositions were set as $x$$BiFeO_3$–$(1 - x)$$YFeO_3$ (where x = 0.1, 0.3, 0.4, 0.5, 0.6, 0.7, and 0.9), labeled from BYFO-01 to BYFO-09. Glycine was used as a reducing agent for the combustion reaction. The average crystallite size of the obtained materials was in the range of 25–90 nm. A study of the magnetic characteristics and photocatalytic activity of the samples showed that variations in their phase composition significantly enhance both the total magnetization and the photodegradation of rhodamine B dye. All samples exhibit magnetic ordering at room temperature and increased magnetization compared to pure bismuth and yttrium orthoferrites. It was found that the BYFO-04 nanocomposite possesses enhanced photocatalytic activity, which was attributed to the approximately 1 : 1 orthoferrite phase ratio. The BYFO-0.5 and BYFO-0.7 nanocomposites showed an improved magnetic response, with specific and saturation magnetization values of approximately 8 emu g^{-1} at a field of 4 kOe. The increased magnetization of these samples was explained by their phase composition, which can be technologically controlled. The discovered properties of the synthesized materials are promising for the effective separation of photocatalysts from the reaction medium. The BYFO-0.4 sample photodegraded about 40% of the rhodamine B dye and 80% of methyl violet within 180 minutes of irradiation with visible light. The easy synthesis method, combined with the magnetic and photocatalytic responses and environmentally benign iron sources, makes $BiFeO_3$–$YFeO_3$ nanocomposites promising materials for photocatalytic systems and memory recording applications.

Received 2nd February 2026,
Accepted 22nd April 2026

DOI: 10.1039/d6ma00153j

rsc.li/materials-advances

1. Introduction

Recent research on multiferroics has focused on orthoferrites $AFeO_3$ (A = Bi, Y) due to their promising magnetic and electrical characteristics, and photocatalytic activity.[1–16] At present, orthoferrites $BiFeO_3$ and $YFeO_3$ are used as materials for magnetic storage devices,[1,2,4,8,9] gas sensors,[2,4] photocatalytic systems,[3,5–7,9,10,17,18] *etc.*

Bismuth orthoferrite ($BiFeO_3$) is a popular magnetoelectric material because it exhibits multiferroic properties at room temperature and above. $BiFeO_3$ has the Néel temperature of $T_N \approx 360$ °C and a Curie temperature of $T_C \approx 830$ °C.[9] Below T_C, bismuth orthoferrite exists in the form of an α-phase with a rhombohedral perovskite-like crystal structure ($R3c$ space group).[19] This material combines the properties of ferroelasticity, antiferromagnetism and ferroelectricity.[2,9] The magnetic nature of $BiFeO_3$ is described as a G-type antiferromagnetic order of Fe^{3+} ions with a space-modulated cycloid spin structure having a period $\lambda_c = 62 \pm 2$ nm.[2] $BiFeO_3$ nanocrystals exhibit weak ferromagnetism arising from the canting of the antiferromagnetic Fe sublattices and the appearance of the Dzyaloshinskii–Moriya effect.[9,13]

Yttrium orthoferrite ($YFeO_3$) is an attractive material due to its excellent magneto-optical properties and extraordinary domain wall motion.[20] In addition, the coupling of magnetic and ferroelectric ordering in $YFeO_3$ makes us consider this compound as a promising multiferroic.[21]

---

[a] *Hydrogen Energy Laboratory, Ioffe Institute, St. Petersburg 194021, Russia*
[b] *Laboratory of Kinetic Phenomena in Solids at Low Temperatures, Ioffe Institute, St. Petersburg 194021, Russia*
[c] *RITVERC JSC, St. Petersburg 194223, Russia*
[d] *Mössbauer Spectroscopy Laboratory, Institute for Analytical Instrumentation of RAS, St. Petersburg 198095, Russia*
[e] *Center of Physical Chemical Methods of Research and Analysis, Al-Farabi Kazakh National University, Almaty 050040, Kazakhstan*
[f] *Department of Materials Science and Engineering, University of Virginia, Charlottesville 22904, USA. E-mail: rvd9ar@virginia.edu*
[g] *Laboratory of New Inorganic Materials, Ioffe Institute, St. Petersburg 194021, Russia. E-mail: natus@mail.ioffe.ru*

One of the ways to improve the performance of the orthoferrites is to create nanocomposite materials, *i.e.*, of systems that include two or more components.[13–16,22–29] Recently, the development of nanocomposites has become a key area in the research of advanced multiferroics. Of particular interest are materials with magnetic order at room temperature. Moreover, nanocomposites can have improved photocatalytic activity due to the formation of new active centers. The synthesis and properties of nanocomposite materials based on bismuth and yttrium orthoferrites with different phase compositions have been described in ref. 14, 24 and 27–31. Most researchers indicate that composite materials based on orthoferrites have improved magnetic and photocatalytic responses and can be synthesized using soft chemical methods. Nanomaterials based on bismuth and yttrium orthoferrites are photocatalysts whose performance can be enhanced by doping.[22] These materials have proven to be very useful for the degradation of dyes under visible light irradiation among other photocatalysts.

Solution combustion synthesis is an effective method for the synthesis of oxide nanoparticles and nanocomposites since it is an energy- and time-saving method that does not require expensive equipment.[13,14,32–40] Currently, this technique is actively used for the synthesis of orthoferrites (*e.g.* ref. 3, 13, 14, 27, 30, 32 and 39–46). The conditions of synthesis, such as the type of organic fuel and the ratio of fuel to oxidizer, strongly affect the formation and properties of oxide nanomaterials,[39,41,42,45,46] including $BiFeO_3$ and $YFeO_3$.

The available data on the properties of the $Bi_{1-x}Y_xFeO_3$/$Y_{1-x}Bi_xFeO_3$ materials are fragmentary and apply only to some compositions. Materials based on the $BiFeO_3$–$YFeO_3$ system are presented in the literature, mainly as solid solutions of the $Bi_{1-x}Y_xFeO_3$/$Y_{1-x}Bi_xFeO_3$ type with a narrow range of $x < 0.3$.[5,47–51] It is noted that with increasing doping, the magnetic response and photocatalytic activity of the $Bi_{1-x}Y_xFeO_3$ materials improve.[47,48,51] The successful synthesis of phases in the range $0 < x < 1$ has apparently been reported only in ref. 52, and the functional properties of most samples have not been studied. There are no publications devoted to the magnetic study of $BiFeO_3$–$YFeO_3$ nanocomposites. The increased photocatalytic activity of Y-doped nanocomposites is reported in ref. 5 and 51. Based on the data on doped materials and pure orthoferrites, we hypothesize that the $BiFeO_3$–$YFeO_3$ system may yield new materials with magnetic order at room temperature and enhanced magnetic and photocatalytic responses.

The aim of this study is to synthesize $BiFeO_3$–$YFeO_3$ nanocomposites *via* glycine–nitrate combustion synthesis and analyze the obtained materials in terms of their magnetic and photocatalytic applications.

2. Materials and methods

2.1. Materials and reagents

Nanocomposites based on the $BiFeO_3$–$YFeO_3$ system were synthesized *via* the glycine–nitrate combustion method. Crystallohydrates of metal nitrates $Bi(NO_3)_3 \cdot 5H_2O$, $Y(NO_3)_3 \cdot 6H_2O$, $Fe(NO_3)_3 \cdot 9H_2O$, and glycine $C_2H_5NO_2$ of p.a. purity grade were used as initial reagents. Metal nitrates were mixed in a proportion corresponding to the nominal compositions of xBiFeO$_3$–$(1 - x)$YFeO$_3$ with $x = 0.1$, 0.3, 0.4, 0.5, 0.6, 0.7, and 0.9.

2.2. Material synthesis procedure

The amount of glycine used as an organic fuel corresponded to a glycine–nitrate (G/N) ratio of 0.55. Metal nitrates and glycine were dissolved in 100 ml of 1 M HNO_3 aqueous solution with constant stirring and heating. The obtained solutions were heated until the water evaporated and the reaction mixtures spontaneously combusted, resulting in the formation of brown powders. The combustion products were sequentially calcined in the temperature range of 350–750 °C for 1 hour at each stage.

Thus, reference samples of $BiFeO_3$ (BFO) and $YFeO_3$ (YFO) were synthesized, as well as a series of xBiFeO$_3$–$(1 - x)$YFeO$_3$ (x = 0.1, 0.3, 0.4, 0.5, 0.6, 0.7, and 0.9) samples. The mixes of Bi–Y orthoferrite samples were named according to the Y content – from BYFO-01 to BYFO-09. The prepared samples were characterized by the following physicochemical methods.

2.3. Material characterization

The morphology of the samples was studied by scanning electron microscopy (FEI Quanta 200 SEM with the EDAX attachment), and the elemental composition of the samples was checked by energy dispersive X-ray analysis.

The powder X-ray diffraction (XRD) patterns of the samples were measured at room temperature by using a CuKα X-ray source (Rigaku SmartLab 3) for the Bragg angle (2θ) range of 20–70°. To calculate the unit cell parameters, the SmartLab software package was used.

A Wissel spectrometer with a ^{57}Co source in a rhodium matrix was used for the Mössbauer examination of the sample at room temperature (isomeric shifts IS are given relative to the IS of α-Fe). Spectra fittings were made with the Mossfit software.

Magnetic measurements were performed with the physical properties materials system (PPMS) provided by quantum design using the vibrating sample magnetometer option. At room temperature, the dependence of the specific magnetization M on the field H was studied. For single-phase samples, they were measured up to 40 kOe, and for nanocomposites – up to 4 kOe.

The photocatalytic activity was assessed by photodegradation of the rhodamine B dye (RdB) under the action of visible light. 30 mg of the photocatalyst was added to a solution of 10 mg L^{-1} RdB, and the resulting mixture was treated with ultrasound for 3 min to achieve maximum dispersion. To increase the photocatalytic activity (photo-Fenton-like mode), 1 mL of 3% H_2O_2 was added. Before irradiation, the mixture was stirred for 60 minutes without light, and then the degree of dye adsorption and desorption on the catalyst surface was determined.

The visible light source was a 300 W Osram Vita-lux lamp with a UV filter. The irradiation intensity in all experiments was 15 mW cm^{-2}. The probes were taken every 30 minutes, and the powders were separated from them by a centrifuge. The rate of photocatalytic degradation of RhB was estimated from the change with time in the absorption spectrum of the solutions. The maximum absorption of RhB is at a wavelength of 550 nm. The absorption spectrum of the solutions was determined on an EMC-11-UV spectrophotometer.

The light absorption ability of the samples was investigated by diffuse reflectance spectra (DRS) in the UV-visible region recorded at room temperature in the range of 400–800 nm using an AvaSphere-30-Refl integrating sphere.

The band gap energy (E_g) was calculated from the plot of the Kubelka–Munk function:

$$F(R) = \frac{(1-R)^n}{2R} = \frac{K}{S} \tag{1}$$

where K is the molar absorption coefficient, S is the scattering factor, and R is the reflectance of the material. The n value is determined by the nature of the sample ($n = 2$ for direct allowed transitions and $n = 1/2$ for indirect allowed transitions).

For statistical analysis of the entire volume of the obtained data, the Pearson matrix was used. For the machine analysis of the dependence of the functional characteristics of $BiFeO_3$–$YFeO_3$ nanocomposites on the composition, variables reflecting the content of bismuth and yttrium were used. The experimentally measured parameters characterizing the photocatalytic properties (reaction rate constant k, min^{-1}; degree of adsorption; time to reach 10% degradation $t_{10\%}$, min; removal efficiency RE; final dye concentration C_{final}, g L^{-1}; amount of reacted substance C_{reacted}, g L^{-1}) and magnetic parameters (excess iron Fe_{excess}; magnetization M, emu g^{-1} at 4 kOe; residual magnetization M_r, emu g^{-1}; coercive force H_c, kOe) were used as response variables. Eight models were used to describe the relationships between composition and functional properties: a classical polynomial regression model and seven machine learning algorithms: CatBoost, Gaussian process regression (GPR), ElasticNet-poly, ElasticNet, eXGBoost, eLasso, and a support vector machine (SVR). Model evaluation was performed using the coefficient of determination.

3. Results and discussion

3.1. Energy-dispersive X-ray (EDX) spectroscopy and scanning electron microscopy (SEM)

The morphology and elemental composition were investigated by SEM/EDXS. The EDX spectra of two typical samples (BYFO-03-09) are shown in Fig. S1 and indicate that the prepared materials contain only the desired Bi, Y, Fe, and O elements. Elemental analysis of the BFO and YFO samples showed that the metal ratio was 1 : 1, *i.e.*, it corresponded to the $BiFeO_3$ and $YFeO_3$ stoichiometry (see Table S1).

Additionally, samples BFO, BYFO-01, and BYFO-09 have average element ratios of Bi/Y/Fe that are fairly close to the nominal values. An excess of iron (d) was detected in the BYFO-03-07 samples that had the highest concentration of iron-containing impurities (Fig. S1) (see Table S2).

Fig. S2 presents SEM images of the samples. It can be seen that the BFO morphology is a network of sintered grains with a rhombic-like shape. With changes in the phase and elemental composition of the materials, the grain morphology becomes less ordered. Doped samples have porous grains with cavities that were formed due to the rapid release of the combustion gases.

The grain size was determined by measuring a substantial number of grains in the SEM images. Y-doping leads to a decrease in particle size and a change in morphology. Thus, samples BYFO-01-04 consist of porous agglomerates of elongated particles, and their micrographs indicate that the grain size is reduced three times (Table S1).

Yttrium ions are less mobile than Bi^{3+} ions, and they slow down the solid-state reaction during sequential heat treatment of the samples, preventing grain growth. The synthesis temperature of these materials was 750 °C, compared to 550 °C previously used for the glycine–nitrate synthesis of pure $BiFeO_3$.[46]

Many dopants were reported to suppress grain growth, and other authors have also assumed that doped $BiFeO_3$ may require slightly higher sintering temperatures. A similar particle morphology was observed in ref. 48, with yttrium doping up to 10%. With a subsequent increase in yttrium content, the particles become flake-shaped and aggregate into disordered porous particles, the size of which increases with increasing Y (see Fig. 2 and Table S2, samples BYFO-06-09). The pure YFO sample consists of highly aggregated flake-like particles with an average grain size of 2.1 μm, which is the maximum for all series of samples.

3.2. Powder X-ray diffraction (PXRD)

The selection of nanocomposite synthesis regime was based on previous data on pure $BiFeO_3$ with enhanced magnetic and photocatalytic characteristics.[37] The samples were sequentially heat-treated in the range of 350–750 °C. After annealing at 750 °C, the samples contained minimal amounts of impurity phases.

Fig. 1 shows the XRD patterns of the samples after final heat treatment at 750 °C. The observed X-ray reflections of the main phase in the BFO and BYFO-01 samples correspond to bismuth orthoferrite $BiFeO_3$. The peaks in these PXRD patterns can be indexed to the rhombohedral, distorted perovskite-like structure (PDF #14-181). In the BYFO-09 and YFO samples, the main phase is perovskite-like yttrium orthoferrite. The reflections in their PXRD patterns correspond to orthorhombic phase $YFeO_3$ (PDF #8-150). The crystallite sizes of the main phases in these samples are given in Table S1. The obtained results are consistent with other works,[5,51] and indicate the formation of $Bi_{1-x}Y_xFeO_3/Y_{1-x}Bi_xFeO_3$ solid solutions at values of $x \leq 0.1$.

The observed X-ray reflections for the BYFO-03-07 samples correspond to a mixture of the main phases, $BiFeO_3$ and $YFeO_3$. Along with these phases, almost all samples contain traces of bismuth ferrites with sillenite-like ($Bi_{25}FeO_{39}$) and mullite-like ($Bi_2Fe_4O_9$) structures. These composite materials likely contain small amounts of iron oxides. Specifically, the BYFO-03-07 samples contain a small amount of magnetite Fe_3O_4, which exhibits a weak characteristic (311) peak around 35.4°. Detailed information on the phase composition of the synthesized samples is presented in Fig. 2.

The causes of the formation of the composites in the intermediate region of yttrium concentration may be the following: firstly, the bismuth content decreases with increasing yttrium

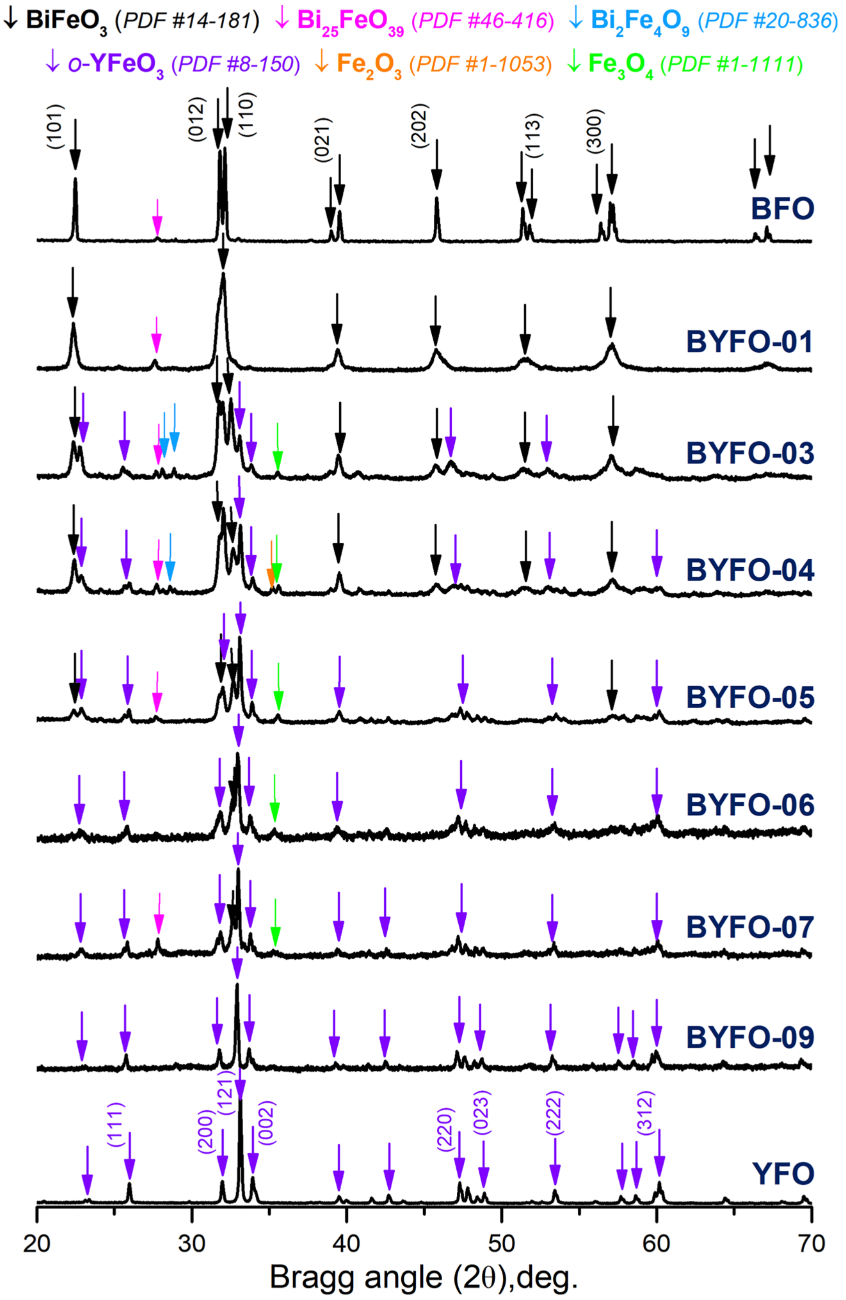

Fig. 1 PXRD patterns of the BFO-YFO samples after heat treatment at 750 °C.

content in these materials, and besides, Bi_2O_3 evaporation begins above 700 °C. Therefore, an excess amount of bismuth nitrate in the initial composition might be required to avoid the formation of secondary phases.

According to ref. 47, the appearance of these by-products could also be caused by lattice strain resulting from the ionic size mismatch between the host and substituent cations. The effective ionic radius of Y^{3+} (1.02 Å for coordination number CN = 8) is smaller than that of Bi^{3+} (1.17 Å in the same coordination).[53] To further clarify the phase composition of the synthesized materials, the data from ^{57}Fe Mössbauer spectroscopy are presented in the following subsection.

The average crystallite sizes (d) of the synthesized particles were estimated from the XRD patterns using the Scherrer equation and are given in Table S1. The calculation was performed using the most intense reflections of the primary phases, $BiFeO_3$ (012/110) and o-$YFeO_3$ (121/002). The average crystallite sizes vary depending on the phase composition, which may be due to spatial limitations on their growth. The estimated d values for the orthoferrites $BiFeO_3$ and $YFeO_3$ are 87 nm and 71 nm, respectively (see Table S1). The crystallite size in the doped materials is smaller than in the pure orthoferrite samples, as can be seen for samples BYFO-01 and BYFO-09. In addition, we did not observe significant differences in the crystallite size for

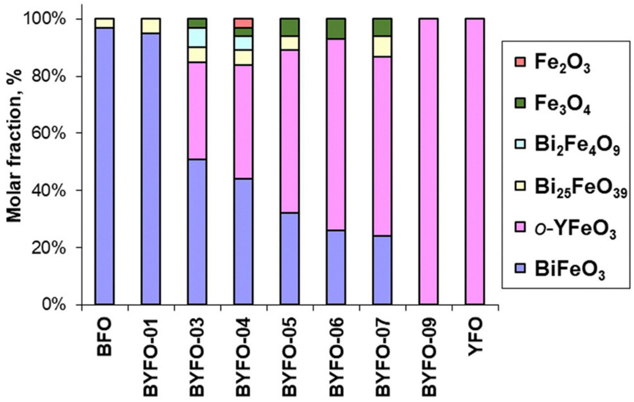

Fig. 2 Phase composition of the BFO-YFO samples.

the BYFO-01 and BYFO-09 samples or the composite samples. The lack of a clear dependence of *d* value on the sample composition may be caused by the overlap of diffraction lines from the main phases, making their precise separation difficult.

3.3. ^{57}Fe Mössbauer spectroscopy

^{57}Fe Mössbauer spectra of the BFO, BYFO-05, BYFO-09, and YFO samples are shown in Fig. 3. As determined from the spectra, the synthesized materials contain magnetically ordered phases at room temperature. The spectra of the BFO and YFO samples consist of sextets, with parameters characterizing the state of iron ions in the magnetically ordered $BiFeO_3$ and $YFeO_3$ phases, respectively.[42,45,46] The spectra of composite samples BYFO-05 and BYFO-09 represent a superposition of sextets and doublets. The parameters of the two doublets in these spectra correspond to octahedrally coordinated Fe^{3+} ions in superparamagnetic $BiFeO_3$ particles and paramagnetic (or non-magnetic) iron species.

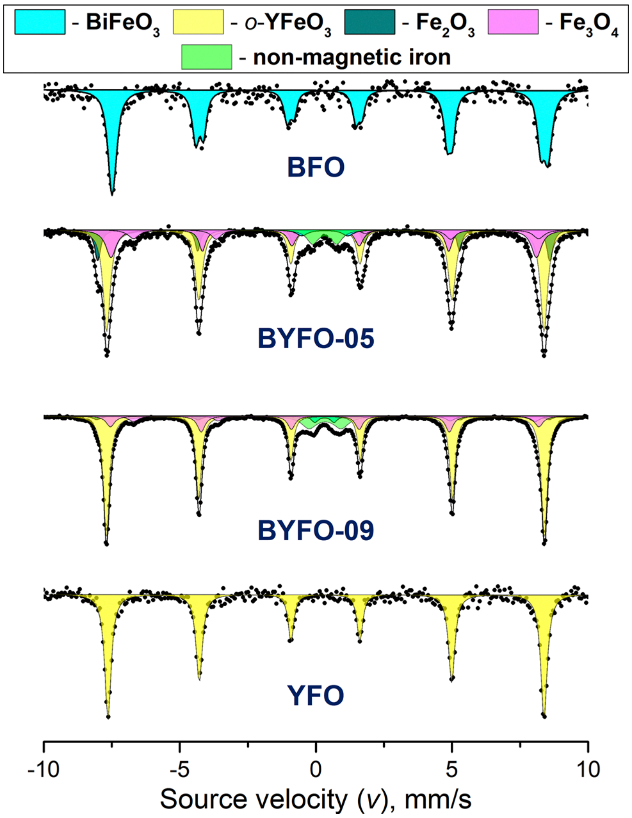

Fig. 3 ^{57}Fe Mössbauer RT-spectra of the BFO, BYFO-05, BYFO-09, and YFO samples.

Comparing the results of XRD and ^{57}Fe Mössbauer spectroscopy, it is clear that the BYFO-04-09 samples contain several iron-containing phases: orthoferrites $BiFeO_3$ and $YFeO_3$, Fe_2O_3 and Fe_3O_4 iron oxides, and a phase with non-magnetic iron. In the BYFO-05 and BYFO-09 samples, the majority of the iron atoms can be attributed to the magnetically ordered $YFeO_3$ phase, the content of which is higher in the BYFO-09 sample. Table S3 summarizes the spectral parameters of the primary phases in comparison with the literature data.

3.4. PPMS vibrational magnetometry

The magnetization (*M*) of the orthoferrite samples as a function of the magnetic field (*H*) at 300 K is shown in Fig. 4a. The hysteresis loops were recorded at room temperature (RT). The presence of these hysteresis loops indicates that both BFO and YFO materials exhibit magnetic ordering at RT.

Nanocrystalline $BiFeO_3$ has a narrow hysteresis loop and non-zero magnetization. The non-saturating behavior of the loop implies the presence of competing antiferromagnetic interactions in the $BiFeO_3$ nanoparticles that have an ordered AFM core and uncompensated spins at the surface of the nanocrystals.[54] Surface magnetization contributes to the total magnetic response of the $BiFeO_3$ nanoparticles, and such materials can exhibit significantly higher magnetization compared to bulk samples.[9] In our case, the average size of the $BiFeO_3$ crystallites is slightly larger than the period of the spin cycloid $d > \lambda_c$ (see Table S1), as a result of which this sample exhibits only a small magnetic response, which is consistent with other studies.[4,9,39]

The YFO sample displays magnetic properties typical of nanocrystalline yttrium orthoferrite obtained by glycine–nitrate combustion. At RT, weak ferromagnetic behavior is observed, resulting from spin canting in the antiferromagnetically ordered Fe^{3+} sublattice, which is caused by Dzyaloshinskii–Moriya interactions. The magnetic hysteresis loop shows low remanent magnetization (M_r = 1.0 emu g^{-1}) and high coercivity (H_c = 23 kOe), indicating strong magnetic anisotropy. The plate-like morphology of the crystallites with an average size of 40 nm contributes to the magnetic hardness of the sample. These results confirm the presence of magnetic ordering at RT, consistent with previously reported data for nanocrystalline $YFeO_3$.

The magnetization curves *M*(*H*) of the nanocomposite, in comparison with orthoferrite samples, are shown in Fig. 5b. The *M*(*H*) curves of the BYFO samples exhibit general similarity and include hysteresis loops, indicating a consistent type of magnetic ordering at RT. Furthermore, the *M*(*H*) curves of the nanocomposites approach saturation at approximately 5 kOe, which qualitatively distinguishes them from the $BiFeO_3$ and $YFeO_3$ curves.

It can also be seen that the BYFO-04-09 samples exhibit a significantly higher total magnetization *M* compared to the

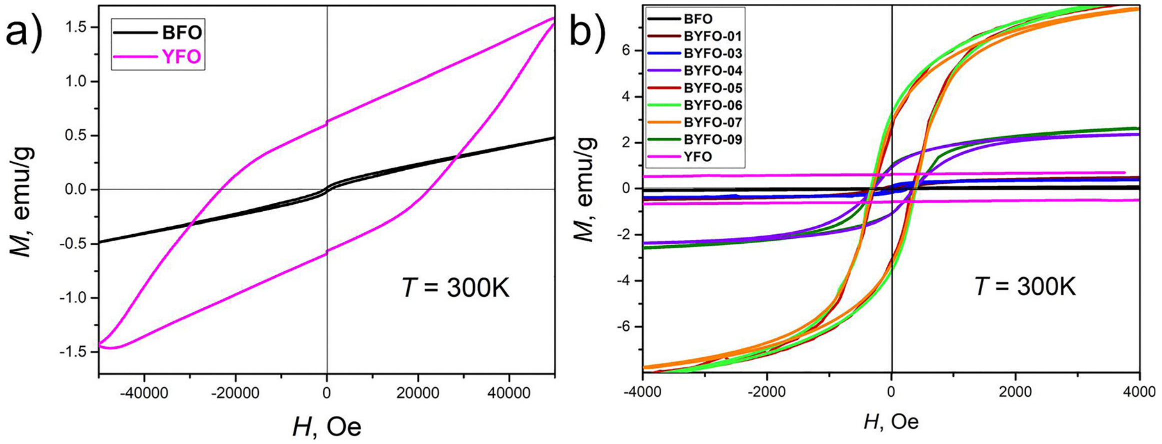

Fig. 4 RT magnetic hysteresis loops of the pure BFO, YFO (a) and BYFO (b) samples.

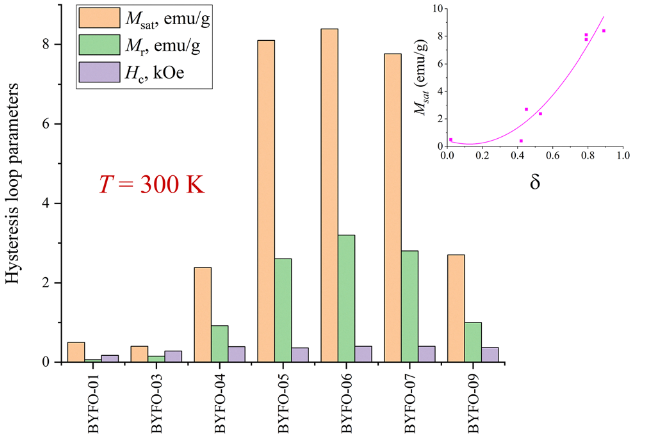

Fig. 5 Remnant magnetization M_r, saturation magnetization M_{sat} and coercivity H_c of the BYFO samples. Inset: M_{sat} measured at 4 kOe as a function of δ.

pure orthoferrite samples. Among them, the BYFO-05, -06, and -07 samples show the highest magnetic response. These samples with enhanced magnetization contain an excess of iron (see Table S2) and impurities of iron-containing magnetic phases (Fig. 1). Analysis of the Mössbauer spectra revealed that the BYFO-05-06-07 samples have a higher proportion of sextets corresponding to the Fe^{3+} states in magnetite Fe_3O_4, which likely enhances the net magnetic response of these composites. In this regard, ferrimagnetism is the most probable type of ordering contributing to the enhanced magnetic response of these materials. It should be noted that the shape of the curves for all doped samples is similar to the $M(H)$ curve of $BiFeO_3$, but with a significantly higher M values (the $M(H)$ curves show a characteristic loop curvature in low fields). This suggests a similar magnetic behavior of the primary phase, while the overall response is dominated by the secondary magnetic inclusions.

In typical $Bi_{1-x}Y_xFeO_3$ solid solutions, the magnetization usually does not exceed 1–2 emu g^{-1}, as it originates solely from canted antiferromagnetism. However, the observed $M_s \sim$ 8 emu g^{-1} are characteristic of ferrimagnetic inclusions, such

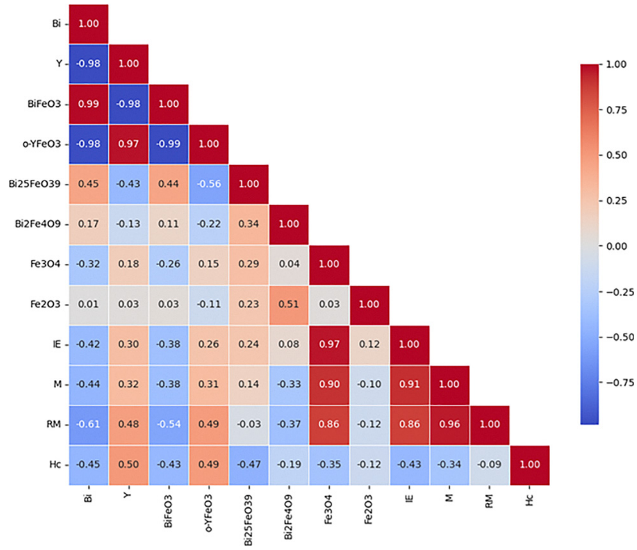

	Bi	Y	BiFeO3	o-YFeO3	Bi25FeO39	Bi2Fe4O9	Fe3O4	Fe2O3	IE	M	RM	Hc
Bi	1.00											
Y	-0.98	1.00										
BiFeO3	0.99	-0.98	1.00									
o-YFeO3	-0.98	0.97	-0.99	1.00								
Bi25FeO39	0.45	-0.43	0.44	-0.56	1.00							
Bi2Fe4O9	0.17	-0.13	0.11	-0.22	0.34	1.00						
Fe3O4	-0.32	0.18	-0.26	0.15	0.29	0.04	1.00					
Fe2O3	0.01	0.03	0.03	-0.11	0.23	0.51	0.03	1.00				
IE	-0.42	0.30	-0.38	0.26	0.24	0.08	0.97	0.12	1.00			
M	-0.44	0.32	-0.38	0.31	0.14	-0.33	0.90	-0.10	0.91	1.00		
RM	-0.61	0.48	-0.54	0.49	-0.03	-0.37	0.86	-0.12	0.86	0.96	1.00	
Hc	-0.45	0.50	-0.43	0.49	-0.47	-0.19	-0.35	-0.12	-0.43	-0.34	-0.09	1.00

Fig. 6 Pearson's correlation matrix for magnetic properties.

as Fe_3O_4 clusters. Since M_s correlates with the iron excess rather than with the yttrium molar fraction (x), these materials can be considered as nanocomposites consisting of the original bismuth and yttrium orthoferrites and magnetic iron oxides.

The physical mechanism underlying this effect in nanocomposites based on bismuth orthoferrite is the partial exchange coupling of magnetic states between $BiFeO_3$ to other magnetic components of the nanocomposite through their interfaces.[27,28] A model describing the interaction between the magnetic moments of $Bi_2Fe_4O_9$ and the local uncompensated moments of the antiferromagnetic $BiFeO_3$, mediated by a spin glass interface, was proposed in ref. 27. Since the BYFO nanocomposites exhibit a more complex phase composition, the exact nature of their magnetization requires further elucidation.

The hysteresis loop parameters for the BYFO samples are shown in Fig. 6. At room temperature, remarkably high values of saturation magnetization (M_{sat}) and remanent magnetization (M_r) were recorded for the BYFO-05-07 samples. This can be attributed to the iron excess δ and the increased concentration of magnetic phases in these samples (Fig. 1). The $M_{sat}(\delta)$ curve is shown in the inset of Fig. 5.

Given that the Y ion is diamagnetic and possesses no intrinsic magnetic moment, the μ_B/Y value represents the degree of local decompensation within the iron antiferromagnetic sublattice induced by the dopant. M_{sat} is strongly dependent on δ rather than the yttrium concentration alone. To gain deeper insight into the origin of magnetism in the BYFO system, the effective magnetic moment per yttrium dopant ion (μ_B/Y) was calculated (see Table S2). The calculation of μ_B/Y showed no systematic trend, confirming that the $Bi^{3+} \rightarrow Y^{3+}$ substitution plays a secondary role in the macroscopic magnetic response compared to parameter δ. The peak observed at $x = 5$ (8.1 emu g^{-1}) coincides with the maximum iron excess in this sample, suggesting the formation of uncompensated iron spin clusters that overshadow the intrinsic weak ferromagnetism of the parent phase. The H_c value also increases with increasing iron content in the samples. At $x > 0.5$ and $\delta > 0.5$, the H_c value ceases to depend on the composition of the samples.

The presence of secondary magnetic phases significantly affects the M_{sat} value, which reaches its maximum in the BYFO-05 and BYFO-06 samples. For these samples, the maximum magnetization was found to be approximately 8 emu g^{-1} at RT. As the δ value increases, M_{sat} sharply increases (see inset to Fig. 6). This behavior of the M_{sat} value correlates well with the XRD and Mössbauer data discussed above. By tuning the initial composition, we can control the parameter δ and magnetic response of the samples. This provides a pathway to developing new materials with enhanced magnetization, which are potentially useful for nonlinear magnetic media.

To establish the relationships between the composition, phase structure, and magnetic properties of the $BiFeO_3$–$YFeO_3$ nanocomposites, a correlation and regression analysis was performed using experimental data and modeling results (Fig. S3). According to the Pearson pair correlation coefficients (PCC), the bismuth content demonstrates a strong positive correlation with the $BiFeO_3$ phase (PCC = 0.99) and a strong negative correlation with *o*-$YFeO_3$ (PCC = −0.98). At the same time, for all measured magnetic parameters – iron excess (Fe_{excess}), magnetization (M), remanent magnetization (M_r), and coercivity (Hc) – the bismuth content correlates negatively (PCC from −0.42 to −0.61). In contrast, the yttrium content has a negative correlation with $BiFeO_3$ (PCC = −0.98) and a positive correlation with *o*-$YFeO_3$ (PCC = 0.97), and also correlates positively with all magnetic properties (PCC from 0.30 to 0.50). This indicates that an increase in the $YFeO_3$ content promotes an increase in magnetization and remanent magnetization, which is consistent with experimental observations: maximum values of $M \approx 8$ emu g^{-1} at 4 kOe and $M_r \approx 3$ emu g^{-1} were recorded at $x = 0.5$–0.7.

Iron-containing secondary phases, which form in composites of intermediate composition, have the greatest influence on the magnetic properties. The strongest correlations are observed for magnetite Fe_3O_4, which is positively correlated with Fe_{excess} (PCC = 0.97), M (0.90), and M_r (0.86), and only weakly negatively correlated with H_c (−0.35). This confirms that the presence of the ferrimagnetic Fe_3O_4 phase is the main factor enhancing the magnetic response and increasing the total magnetization in the BYFO-05-07 composites. In addition, the *o*-$YFeO_3$ phase shows positive correlations with M_r (0.49) and H_c (0.49), reflecting the contribution of crystalline anisotropy and spin canting to the increase in coercivity. In contrast, $BiFeO_3$ exhibits a negative correlation with M_r (−0.54), and the $Bi_{25}FeO_{39}$ phase with H_c (−0.47), indicating their paramagnetic or weakly ferromagnetic nature, which reduces the overall magnetic response of the composite. Eight models, including polynomial regression and machine learning methods, were used to quantitatively evaluate the relationships between composition and magnetic properties (Fig. S3). The CatBoost and GPR models demonstrated the highest accuracy values ($R^2 = 1.0$) for all parameters, indicating a high adequacy of the nonlinear description of the dependencies. The polynomial model also provided good results for Fe excess ($R^2 = 0.93$), M_r (0.91), and M (0.84), confirming the presence of quadratic components in the composition-dependent properties. The eXGBoost and SVR models showed satisfactory results ($R^2 = 0.50$–0.95), while the linear ElasticNet and eLasso models did not capture the relationship ($R^2 \approx 0$), indicating the complex nonlinear nature of the magnetic behavior of the composite. A combined analysis of correlations and modeling shows that enhanced magnetic properties are observed with increasing yttrium content and the formation of Fe_3O_4 and *o*-$YFeO_3$ phases, while the predominance of $BiFeO_3$ and $Bi_{25}FeO_{39}$ leads to weakening of the magnetization and coercivity. The most pronounced magnetic characteristics are achieved at a $BiFeO_3 : YFeO_3$ ratio of $\approx 1:1$ ($x \approx 0.5$–0.7), when ferrimagnetic components Fe_3O_4 and Fe_2O_3 form at the phase boundary, facilitating exchange interactions between the spin subsystems. This combination of antiferromagnetic and ferrimagnetic phases ensures the formation of interface-induced ferrimagnetism and explains the nonlinear increase in M and M_r with increasing $YFeO_3$ content.

3.5. Visible-light absorbance and photocatalytic activity

The photocatalytic properties of yttrium-doped bismuth orthoferrites were evaluated by photodegradation of the organic dye RhB in the presence of hydrogen peroxide under visible light. The temporal change in the absorption spectra during the photodegradation of the RhB solution under the influence of the BYFO-04 photocatalyst and H_2O_2 under visible light is shown in Fig. 7a. A slight shift in the main absorption peak was also observed with other samples, indicating the conversion of RhB to Rh-110 during *N*-deethylation indirect photodegradation in the presence of BYFO.[55]

Fig. 7c shows the time dependence of RhB photodegradation in the presence of BYFO photocatalysts and H_2O_2. When adsorption–desorption equilibrium is reached, the highest degree of adsorption is observed in the BYFO-04 sample, which is the best photocatalyst in the BYFO series. This sample photodegraded about 40% of RhB dye within 180 minutes of irradiation with visible light. According to the XRD data, the ratio of the main phases $BiFeO_3$/$YFeO_3$ in this sample is approximately 1 : 1 (Fig. 2). It can be assumed that such a phase ratio ensures the creation of a stable interface between the components of the BYFO nanocomposite,

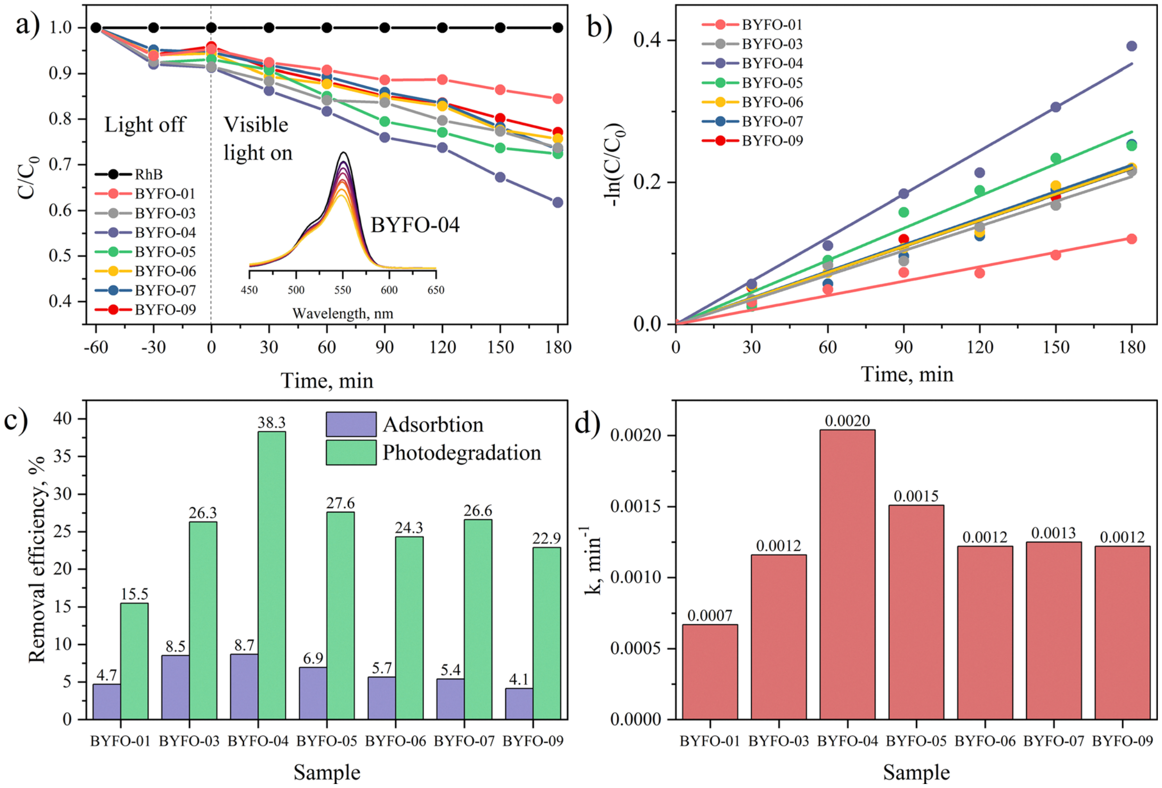

Fig. 7 Photocatalytic performance of the BFO-YFO samples under visible light: (a) Fenton-like degradation of the dye; absorption spectra of RhB decolorization (inset a); (b) pseudo-first-order kinetic plots; (c) removal efficiency during adsorption and photodegradation of RhB; (d) reaction rate constants.

which leads to an increase in its photocatalytic efficiency. A further increase in concentration leads to a decrease in photocatalytic activity and the formation of a plateau in degradation efficiency (Fig. 7b).

One of the possible reasons for the highest photoactivity of the BYFO-04 sample with the addition of hydrogen peroxide to the reaction may be the presence of a photocatalytically active semiconductor Fe_2O_3 in this sample (see Fig. 2). Compared to other samples, the formation of the impurity compound Fe_2O_3 can serve to suppress electron–hole recombination by the effect of capturing electrons from the conduction band by Fe^{3+} ions and further accelerate the Fenton-like reaction by initiating the activation of H_2O_2 with the formation of active $^{\bullet}OH$ radicals,[34] which can be explained by the redox reaction of Fe^{2+}/Fe^{3+} ions illustrated by the equations:

$$H_2O + h^+ \rightarrow {}^{\bullet}OH$$

$$Fe^{3+} + e^- \rightarrow Fe^{2+}$$

$$Fe^{2+} + H_2O_2 \rightarrow Fe^{3+} + OH^- + {}^{\bullet}OH$$

In Fig. 10d, it can be seen that a fairly good linear correlation was found ($R > 0.98$), indicating that the reaction is a pseudo-first order reaction. To quantitatively understand the kinetics of the RhB degradation reaction, a pseudo-first order model expressed by eqn (2), which is typically used at low initial contaminant concentrations, was applied.[56] As stated above, the presence of impurity iron oxides in BYFO-04 leads to an increase in the photodegradation rate constant to $k = 2.04 \times 10^{-3}$ min^{-1}.

$$\ln\left(\frac{C_0}{C}\right) = kt \qquad (2)$$

where C_0 is the initial concentration of the dye, C is the concentration of the dye after t minutes, k is the reaction rate constant (min^{-1}), and t is time.

To determine the compositional dependence of the photocatalytic activity of the $BiFeO_3$–$YFeO_3$ nanocomposites, a correlation and regression analysis was performed using experimental parameters (k, RE, C_{reacted}, C_{final}, $t_{10\%}$, Ads) (Fig. 8). According to the calculations of the Pearson pair correlation coefficients (PCCs), the bismuth content has a strong positive correlation with the $BiFeO_3$ phase (PCC = 0.98) and a strong negative correlation with the o-$YFeO_3$ phase (PCC = −0.97). For photocatalytic parameters, a negative correlation is observed between the bismuth content and the rate constant (k, −0.44), the decomposition efficiency (RE, −0.34), and the amount of reacted substance (C_{reacted}, −0.34), while a positive correlation is observed with the final dye concentration (C_{final}, 0.34), the time to reach 10% degradation ($t_{10\%}$, 0.29), and the degree of adsorption (Ads, 0.19). Thus, an increase in the $BiFeO_3$ proportion is accompanied by a decrease in photocatalytic activity. In contrast, increasing the

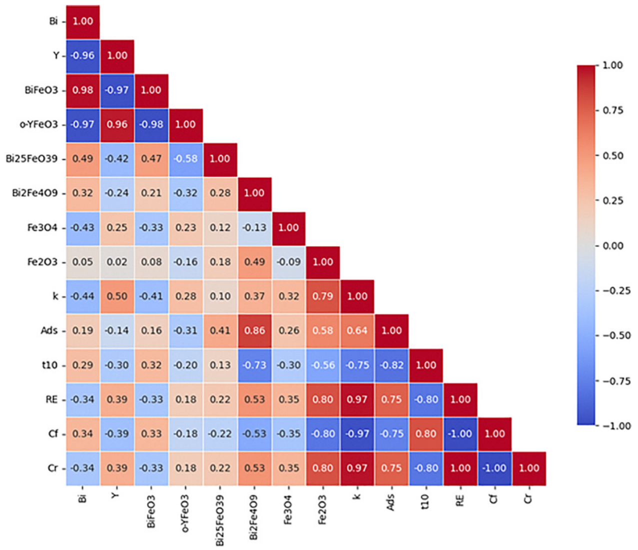

	Bi	Y	BiFeO3	o-YFeO3	Bi25FeO39	Bi2Fe4O9	Fe3O4	Fe2O3	k	Ads	t10	RE	Cf	Cr
Bi	1.00													
Y	-0.96	1.00												
BiFeO3	0.98	-0.97	1.00											
o-YFeO3	-0.97	0.96	-0.98	1.00										
Bi25FeO39	0.49	-0.42	0.47	-0.58	1.00									
Bi2Fe4O9	0.32	-0.24	0.21	-0.32	0.28	1.00								
Fe3O4	-0.43	0.25	-0.33	0.23	0.12	-0.13	1.00							
Fe2O3	0.05	0.02	0.08	-0.16	0.18	0.49	-0.09	1.00						
k	-0.44	0.50	-0.41	0.28	0.10	0.37	0.32	0.79	1.00					
Ads	0.19	-0.14	0.16	-0.31	0.41	0.86	0.26	0.58	0.64	1.00				
t10	0.29	-0.30	0.32	-0.20	0.13	-0.73	-0.30	-0.56	-0.75	-0.82	1.00			
RE	-0.34	0.39	-0.33	0.18	0.22	0.53	0.35	0.80	0.97	0.75	-0.80	1.00		
Cf	0.34	-0.39	0.33	-0.18	-0.22	-0.53	-0.35	-0.80	-0.97	-0.75	0.80	-1.00	1.00	
Cr	-0.34	0.39	-0.33	0.18	0.22	0.53	0.35	0.80	0.97	0.75	-0.80	1.00	-1.00	1.00

Fig. 8 Pearson's correlation matrix for photocatalytic properties.

yttrium content, which correlates negatively with $BiFeO_3$ (PCC = −0.97) and positively with o-$YFeO_3$ (PCC = 0.96), has the opposite effect: for the k, RE, and $C_{reacted}$ parameters, the correlation is positive (0.39–0.50), while for Ads, $t_{10\%}$, and C_{final}, it is negative (−0.14 to −0.39). This indicates that increasing the proportion of $YFeO_3$ and associated oxide phases accelerates photodegradation and increases the efficiency of organic compound decomposition under the influence of visible light.

The contribution of secondary phases should be noted separately. The appearance of the $Bi_2Fe_4O_9$ phase is accompanied by a strong positive correlation with Ads (0.86), RE (0.53), $C_{reacted}$ (0.53) and a negative one with $t_{10\%}$ (−0.73), C_{final} (−0.53), indicating an increase in photo-Fenton-like activity with increasing its content. Similarly, the Fe_2O_3 phase exhibits a positive correlation with Ads (0.58), RE (0.80), $C_{reacted}$ (0.80) and a negative one with $t_{10\%}$ (−0.56), C_{final} (−0.80), confirming its role in accelerating dye degradation processes due to the generation of active $^{\bullet}OH$ radicals.

Eight models, including polynomial regression and machine learning algorithms, were used to quantitatively describe the dependencies (Fig. S4). The best results across all parameters were achieved for the CatBoost (R^2 = 1.0) and GPR (R^2 = 0.94–1.0) models, confirming the presence of pronounced nonlinear relationships between composition and photocatalytic performance. The polynomial model demonstrated high R^2 values for Ads (0.996), k (0.93), $t_{10\%}$ (0.96), and RE (0.89), indicating an adequate description of the effect through a quadratic relationship. The eXGBoost and SVR algorithms showed moderate results (R^2 = 0.45–0.76), while the ElasticNet and eLasso linear models were unable to capture the patterns ($R^2 \approx 0$), confirming the complex nonlinear nature of photodegradation processes in heterogeneous systems. Thus, the simulation confirmed that increasing the yttrium content and the formation of the $YFeO_3$ phase, as well as the presence of photocatalytically active Fe_2O_3 and $Bi_2Fe_4O_9$ phases, contributes to an increase in the degradation rate of organic dyes and an increase in the efficiency of photocatalysis. The highest values of the rate constant ($k = 2.04 \times 10^{-3}$ min^{-1}) and degradation efficiency (RE) are observed in samples with a close ratio of $BiFeO_3 : YFeO_3 \approx 1 : 1$ ($x \approx$ 0.4–0.5), which is consistent with the experimental results and confirms the role of interfacial interactions in enhancing photo-Fenton-like processes.

To assess the practical applicability of the synthesized BYFO-04 photocatalyst, its photocatalytic activity was evaluated using a range of model organic dyes (Fig. 9a–c). The material demonstrated high degradation efficiency toward thiazine and triarylmethane dyes, achieving 65% and 80% decomposition of methylene blue and methyl violet, respectively. In contrast, the degradation efficiency for azo dyes was limited to approximately 25%, which can be attributed to their greater structural stability under the applied conditions. Reaction rate constants are presented in Fig. 9d.

To elucidate the mechanism of the Fenton-like degradation of rhodamine B catalyzed by the synthesized material, a series of radical scavenging experiments were conducted (Fig. 9d and e). Ascorbic acid was employed to scavenge superoxide radicals ($^{\bullet}O_2^{-}$), isopropyl alcohol (IPA) was used to trap hydroxyl radicals ($^{\bullet}OH$), disodium ethylenediaminetetraacetate (EDTA) served as a hole (h^+) scavenger, and potassium dichromate ($K_2Cr_2O_7$) was utilized to capture photogenerated electrons (e^-). The results indicate that hydroxyl radicals ($^{\bullet}OH$) and superoxide radicals ($^{\bullet}O_2^{-}$) play dominant roles in the degradation process, whereas photogenerated holes (h^+) and electrons (e^-) contribute to a lesser extent.[57] Moreover, cycling stability tests revealed a gradual decline in catalytic activity, with an approximate 5% loss in efficiency observed by the fifth cycle (Fig. 9f).

The diffuse reflectance spectra of the samples are presented in Fig. 10a. All the samples demonstrate low reflectance at 400–550 nm that indicates the effective absorbance of the visible light spectrum. The bends of the curves demonstrate the strong interaction with visible light in its full range for all samples. It can be noticed that the reflection rate systematically decreases with increase of the yttrium content, except for the YFO sample. The band gap energy values were evaluated by extrapolation of the linear Tauc plot parts (Fig. 10b) and summarized in Table S4. The band gap energy values (Fig. 9c) for the BFO and YFO samples were 2.0 and 1.94 eV, respectively, which is close to previous reports (4, 14). The E_g values of $BiFeO_3$ slightly increase with increase of the yttrium content up to 2.04 eV, within the error of the determination method. For the o-$YFeO_3$ phase (BYFO-0.3-0.5, 1), there is the same behavior with insignificant change of the band gap energy. However, for several samples (BYFO-0.6-0.9) a noticeable decrease in E_g is observed, which can be associated with their solid-solution nature.

The band gap structure parameters were evaluated by the following empirical formulas: $E_{VB} = \chi - E_e + 0.5{\cdot}E_g$ and $E_{CB} = E_{VB} - E_g$, where E_e = 4.5; χ is the electronegativity, χ (YFO) = 5.60 eV, χ (BFO) = 5.89 eV. The calculated values of the conduction band edge potential (E_{CB}) and valence band edge potentials (E_{VB}) are presented in Table S4, and the band gap structure of Y04 is visualized in Fig. 10.

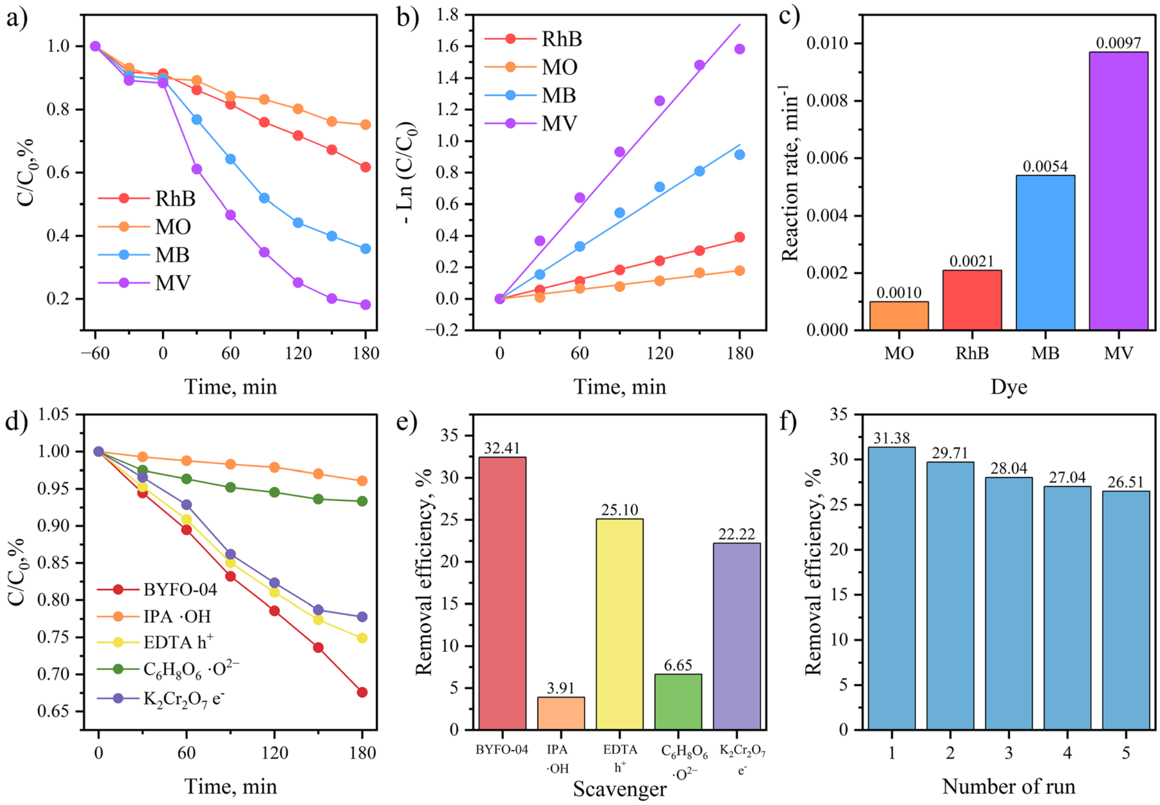

Fig. 9 Photocatalytic performance of the BYFO-04 sample under visible light: (a) Fenton-like degradation of dyes, (b) pseudo-first-order kinetic plots, (c) reaction rate constants, (d and e) scavenger tests for RhG photodegradation, and (f) cyclic stability test.

The activity of both nanocomposite materials under visible light irradiation (E_g(BFO) = 2.04 eV, E_g(YFO) = 1.91 eV) was previously mentioned.

$$\mathrm{BiFeO_3} + h\nu \rightarrow \mathrm{e^-}_{\mathrm{CB}} + \mathrm{h^+}_{\mathrm{VB}}$$

$$\mathrm{YFeO_3} + h\nu \rightarrow \mathrm{e^-}_{\mathrm{CB}} + \mathrm{h^+}_{\mathrm{VB}}$$

The calculated CB and VB values were 0.37 eV and 2.41 eV for BFO, and 0.16 eV and 2.05 eV for YFO providing the heterojunction formation. The possibility of electron transfer from $YFeO_3$ CB to $BiFeO_3$ CB and hole transfer from $BiFeO_3$ VB to $YFeO_3$ VB prevents the coupling of electron–hole pairs and increases photocatalytic activity (Fig. 11). The wide band gaps and high VB values of both nanocomposite components make feasible several •OH radical generation reactions.

$$\mathrm{OH^-} + \mathrm{h^+} \rightarrow {}^{\bullet}\mathrm{OH}$$

$$\mathrm{H_2O} + \mathrm{h^+} \rightarrow {}^{\bullet}\mathrm{OH} + \mathrm{H^+}$$

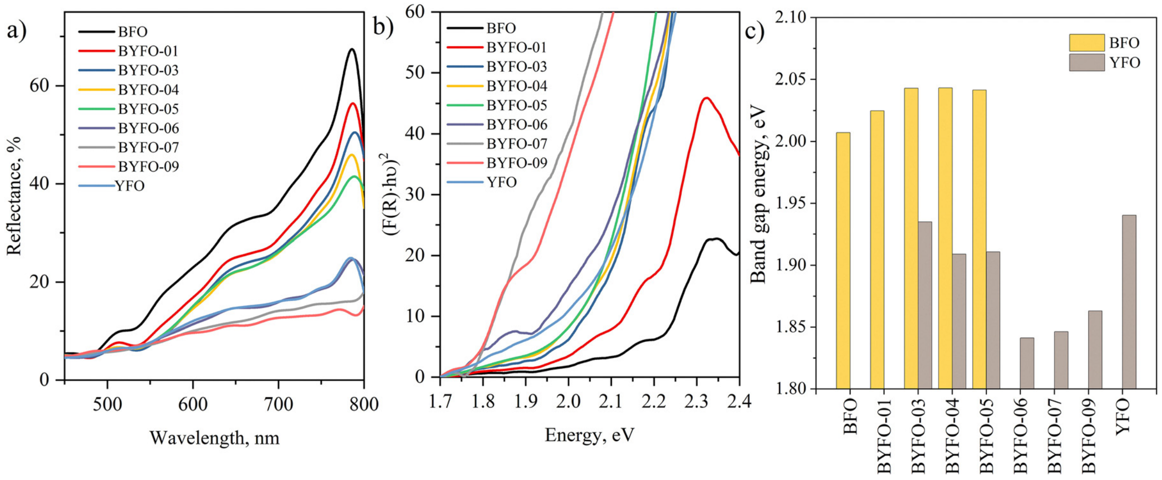

Fig. 10 Diffuse reflectance spectra (a), Tauc plots (b), and band gap energy values (c) of the BFO-YFO samples.

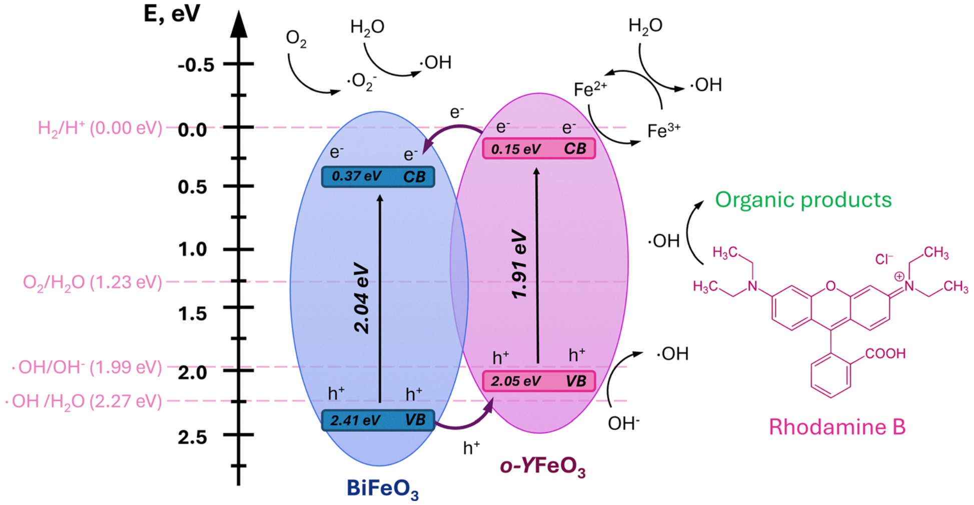

Fig. 11 Mechanism of photo-Fenton degradation of RhB over the BFO–YFO nanocomposites.

$$H_2O_2 + e^- \rightarrow {}^{\bullet}OH + OH^-$$

$$O_2 + e^- \rightarrow {}^{\bullet}O^{2-}$$

$${}^{\bullet}O_2{}^- + H_2O \rightarrow {}^{\bullet}OH_2 + OH^-$$

$${}^{\bullet}OH_2 + {}^{\bullet}OH_2 \rightarrow O_2 + H_2O_2$$

$$H_2O_2 + {}^{\bullet}O^{2-} \rightarrow {}^{\bullet}OH + O_2 + OH^-$$

The ${}^{\bullet}OH$ radicals are known to be very effective in organic pollutant degradation.

$$RhB + {}^{\bullet}OH \rightarrow CO_2 + N_2 + H_2O$$

The presence of Fe^{3+} ions in both nanocomposite materials leads to multiple ${}^{\bullet}OH$ radicals' generation in a Fenton-like process.

$$Fe^{3+} + e^- \rightarrow Fe^{2+}$$

$$Fe^{2+} + H_2O_2 \rightarrow Fe^{3+} + {}^{\bullet}O_2{}^- + H_2O$$

This explains the high photocatalytic activity of the $BiFeO_3$–$YFeO_3$ heterojunction nanocomposite in the process of Fenton-like photodegradation of RhB. The reduced electron–hole pair coupling increased ${}^{\bullet}OH$ radical generation, and the high level of visible light absorption makes this photocatalyst a promising material for advanced oxidation processes in organic pollutant decomposition.

An increase in the photocatalytic activity of the $BiFeO_3$–$YFeO_3$ nanocomposites can be realized by varying the iron content in the target product, which can be influenced by the synthesis conditions, such as the type of organic fuel and the fuel/oxidizer ratio in the initial composition. Properties such as magnetically ordered state at room temperature and obvious photocatalytic activity of the synthesized materials are promising for efficient separation of the photocatalyst from the reaction medium.

4. Conclusion

Nanocrystalline materials based on the $xBiFeO_3$–$(1-x)YFeO_3$ system were synthesized using the glycine–nitrate combustion method. The obtained materials have an average crystallite size in the range of 25–90 nm. XRD and EDX data demonstrated the effect of the initial composition on the phase composition of the target product. At nominal values of $x = 0.3$–0.7, nanocomposite samples were formed. It was found that the BYFO-04 nanocomposite with a ratio of approximately 1 : 1 between bismuth and yttrium orthoferrites exhibits increased photocatalytic activity compared to the other samples.

The magnetic properties of the obtained materials were investigated by Mössbauer spectroscopy and magnetometry. At RT, all synthesized materials exhibit magnetic order. The results showed that the BYFO materials have improved magnetic properties, demonstrating an increase in total magnetization by several times compared to pure orthoferrites. The BYFO-0.5 and BYFO-0.7 nanocomposites showed an improved magnetic response, with specific and saturation magnetization values of approximately 8 emu g^{-1} at a field of 4 kOe. The discovered properties of the synthesized materials are promising for the effective separation of photocatalysts from the reaction medium.

Author contributions

S. M. Tikhanova – formal analysis, investigation, visualization, writing – original draft, and writing – review and editing; M. P. Volkov – data curation, formal analysis, and investigation; I. V. Buryanenko – data curation, formal analysis, and investigation; V. G. Semenov – data curation, formal analysis, and investigation; Z. Orazovd – data curation, formal analysis, and investigation; V. I. Romanovski – data curation, formal analysis, investigation, visualization, writing – original draft, and writing – review and editing; V. I. Popkov – project administration, supervision, validation, and writing – review and editing; N. A. Lomanova – conceptualization, methodology, project administration, supervision, validation, and writing – review and editing.

Conflicts of interest

The authors declare no competing interests.

Data availability

The data that support the findings of this study are available from the corresponding author upon reasonable request.

Supplementary information (SI) is available. See DOI: https://doi.org/10.1039/d6ma00153j.

Acknowledgements

The authors are grateful to Victor V. Gusarov (Ioffe Institute, St. Petersburg, Russia) for fruitful discussions and advice.

References

1 J. F. Scott, Data storage: Multiferroic memories, *Nat. Mater.*, 2007, **6**, 256–257, DOI: 10.1038/NMAT1868;KWRD.

2 A. R. Akbashev, A. R. Kaul, A. R. Akbashev and A. R. Kaul, Structural and chemical aspects of the design of multiferroic materials, *RuCRv*, 2011, **80**, 1159–1177, DOI: 10.1070/RC2011V080N12ABEH004239.

3 Y. Chen, J. Yang, X. Wang, F. Feng, Y. Zhang and Y. Tang, Synthesis $YFeO_3$ by salt-assisted solution combustion method and its photocatalytic activity, *J. Ceram. Soc. Jpn.*, 2014, **122**, 146–150, DOI: 10.2109/JCERSJ2.122.146.

4 N. Wang, X. Luo, L. Han, Z. Zhang, R. Zhang, H. Olin and Y. Yang, Structure, Performance, and Application of $BiFeO_3$ Nanomaterials, *Nano-Micro Lett.*, 2020, **12**, 1–23, DOI: 10.1007/S40820-020-00420-6/FIGURES/3.

5 O. Rosales-González, F. Sánchez-De Jesús, M. A. Camacho-González, C. A. Cortés-Escobedo and A. M. Bolarín-Miró, Synthesis of magnetically removable photocatalyst based on bismuth doped $YFeO_3$, *Mater. Sci. Eng., B*, 2020, **261**, 114773, DOI: 10.1016/j.mseb.2020.114773.

6 V. Venugopal, D. Balaji, M. Preeyanghaa, C. J. Moon, B. Neppolian, G. Muthusamy, J. Theerthagiri, J. Madhavan and M. Y. Choi, Synergistic combination of $BiFeO_3$ nanorods and $CeVO_4$ nanoparticles for enhanced visible light driven photocatalytic activity, *Alexandria Eng. J.*, 2023, **72**, 531–543, DOI: 10.1016/J.AEJ.2023.04.024.

7 L. A. Al-Hajji, H. Alshaikh, M. H. H. Mahmoud and A. A. Ismail, Soft Template-Assisted Controllable Synthesis of Nanocrystalline Orthorhombic $YFeO_3$ Decorated Porous g-C_3N_4 with Enhanced Hg(II) reduction, *J. Inorg. Organomet. Polym. Mater.*, 2021, **31**, 4150–4162, DOI: 10.1007/S10904-021-02022-0/FIGURES/8.

8 G. M. Alsulaim and K. M. Alnahdi, New magnetic nanoscaled AlVCe-Cr_2O_3 semiconductors for opto- and spin-transport electronics, *Alexandria Eng. J.*, 2025, **132**, 169–180, DOI: 10.1016/j.aej.2025.10.029.

9 J. Wu, Z. Fan, D. Xiao, J. Zhu and J. Wang, Multiferroic bismuth ferrite-based materials for multifunctional applications: Ceramic bulks, thin films and nanostructures, *Prog. Mater. Sci.*, 2016, **84**, 335–402, DOI: 10.1016/J.PMATSCI.2016.09.001.

10 X. Li, Z. Tang, H. Ma, F. Wu and R. Jian, PVP-assisted hydrothermal synthesis and photocatalytic activity of single-crystalline $BiFeO_3$ nanorods, *Appl. Phys. A: Mater. Sci. Process.*, 2019, **125**, 1–6, DOI: 10.1007/S00339-019-2892-2/FIGURES/6.

11 T. D. Trinh, N. A. Tien, V. O. Mittova, B. N. V. Phuong, T. T. T. Ngan, T. T. T. Nga, N. Van My, I. Y. Mittova, E. V. Tomina, L. T. T. Thuy and T. S. Cam, Studying the influence of synthesis conditions on the magnetic properties of perovskite-like $YbFeO_3$ nanomaterials, *J. Solid State Chem.*, 2023, **328**, 124377, DOI: 10.1016/J.JSSC.2023.124377.

12 N. A. Tien, N. T. Trang, V. O. Mittova, N. T. Lan, N. T. T. Nhan, C. H. Diem, T. C. Hien, I. Y. Mittova and B. X. Vuong, Structural, thermal, and magnetic properties of orthoferrite $EuFeO_3$ nanoparticles prepared by a simple co-precipitation method, *J. Mater. Sci. Mater. Electron.*, 2023, **34**, 1–10, DOI: 10.1007/S10854-023-10779-Y/TABLES/2.

13 A. S. Seroglazova, M. I. Chebanenko, V. N. Nevedomskyi and V. I. Popkov, Solution combustion synthesis of novel $PrFeO_3$/CeO_2 nanocomposite with enhanced photo-Fenton activity under visible light, *Ceram. Int.*, 2023, **49**, 15468–15479, DOI: 10.1016/J.CERAMINT.2023.01.132.

14 T. S. Cam, A. S. Seroglazova, M. I. Chebanenko, B. Mardiyev, E. V. Dzhevaga, O. V. Almjasheva and V. I. Popkov, Colloidal solution combustion synthesis of am-TiO_2/o-$YFeO_3$ nanocomposites: effect of titania loading on the photo-Fenton-like activity, *J. Sol-Gel Sci. Technol.*, 2023, **108**, 502–513, DOI: 10.1007/S10971-023-06206-7/FIGURES/11.

15 S. Tikhanova, A. Seroglazova, M. Chebanenko, V. Nevedomskiy and V. Popkov, Effect of TiO_2 Additives on the Stabilization of h-$YbFeO_3$ and Promotion of Photo-Fenton Activity of o-$YbFeO_3$/h-$YbFeO_3$/r-TiO_2 Nanocomposites, *Materials*, 2022, **15**(22), 8273, DOI: 10.3390/ma15228273.

16 Y. Albadi, M. S. Ivanova, L. Y. Grunin, R. A. Makarin, A. S. Komlev, M. I. Chebanenko, V. N. Nevedomskyi and V. I. Popkov, Ultrasound-assisted co-precipitation synthesis of $GdFeO_3$ nanoparticles: structure, magnetic and MRI contrast properties, *Phys. Chem. Chem. Phys.*, 2022, **24**, 29014–29023, DOI: 10.1039/D2CP03688F.

17 G. M. Alsulaim, New photocatalysts stimulated by visible light for organic-waste remediation: (La/Ce) and (La/Gd) codoped $BiFeO_3$, *J. Mater. Sci. Mater. Electron.*, 2023, **34**(36), 2290, DOI: 10.1007/s10854-023-11671-5.

18 G. M. Alsulaim, Ferromagnetic nature and solar-induced fast catalytic properties for green environment: New Fe/Cu/V-Mn_3O_4 p-type compounds, *Arab. J. Chem.*, 2025, **18**, 1342025, DOI: 10.25259/ajc_134_2025.

19 D. C. Arnold, K. S. Knight, F. D. Morrison and P. Lightfoot, Ferroelectric-paraelectric transition in $BiFeO_3$: Crystal structure of the orthorhombic β phase, *Phys. Rev. Lett.*, 2009, **102**(2), 027602, DOI: 10.1103/PHYSREVLETT.102.027602.

20 H. Shen, J. Xu, A. Wu, J. Zhao and M. Shi, Magnetic and thermal properties of perovskite $YFeO_3$ single crystals, *Mater. Sci. Eng., B*, 2009, **157**, 77–80, DOI: 10.1016/J.MSEB.2008.12.020.

21 Z. Zhou, L. Guo, H. Yang, Q. Liu and F. Ye, Hydrothermal synthesis and magnetic properties of multiferroic rare-earth orthoferrites, *J. Alloys Compd.*, 2014, **583**, 21–31, DOI: 10.1016/J.JALLCOM.2013.08.129.

22 A. Haruna, I. Abdulkadir and S. O. Idris, Photocatalytic activity and doping effects of $BiFeO_3$ nanoparticles in model organic dyes, *Heliyon*, 2020, **6**, e03237, DOI: 10.1016/J.HELIYON.2020.E03237.

23 K. D. Martinson, V. A. Ivanov, M. I. Chebanenko, V. V. Panchuk, V. G. Semenov and V. I. Popkov, Facile combustion synthesis of $TbFeO_3$ nanocrystals with hexagonal and orthorhombic structure, *Nanosyst. Physics, Chem. Math.*, 2019, **10**, 694–700, DOI: 10.17586/2220-8054-2019-10-6-694-700.

24 Y. Subramanian, V. Ramasamy, R. J. Karthikeyan, G. R. Srinivasan, D. Arulmozhi, R. K. Gubendiran and M. Sriramalu, Investigations on the enhanced dye degradation activity of heterogeneous $BiFeO_3$–$GdFeO_3$ nanocomposite photocatalyst, *Heliyon*, 2019, **5**, e01831, DOI: 10.1016/J.HELIYON.2019.E01831.

25 N. V. Besprozvannykh, D. S. Ershov and O. Y. Sinelshchikova, SrO–BiP_2O_3–Fe_2O_3-Based Composites: Synthesis and Electrophysical Properties, *Russ. J. Gen. Chem.*, 2019, **89**, 2458–2462, DOI: 10.1134/S1070363219120211/METRICS.

26 M. S. Lomakin, O. V. Proskurina, D. P. Danilovich, V. V. Panchuk, V. G. Semenov and V. V. Gusarov, Hydrothermal synthesis, phase formation and crystal chemistry of the pyrochlore/Bi_2WO_6 and pyrochlore/α-Fe_2O_3 composites in the Bi_2O_3–Fe_2O_3–WO_3 system, *J. Solid State Chem.*, 2020, **282**, 121064, DOI: 10.1016/J.JSSC.2019.121064.

27 I. V. Pleshakov, M. P. Volkov, N. A. Lomanova, Y. I. Kuz'min and V. V. Gusarov, Magnetic Characteristics of a Nanocomposite Based on Bismuth Ferrites, *Tech. Phys. Lett.*, 2020, **46**, 1072–1075, DOI: 10.1134/S1063785020110115/FIGURES/3.

28 T. Maity and S. Roy, Asymmetric ascending and descending loop shift exchange bias in $Bi_2Fe_4O_9$-$BiFeO_3$ nanocomposites, *J. Magn. Magn. Mater.*, 2020, **494**, 165783, DOI: 10.1016/J.JMMM.2019.165783.

29 L. Tian, P. Gao, F. Wang, X. Li and G. Li, Study on Preparation of $BiFeO_3$/$Bi_2Fe_4O_9$ Composite Photocatalyst and Photocatalytic Degradation of Various Organic Dyes in Waste Water, *Russ. J. Phys. Chem. A*, 2021, **95**, 1495–1504, DOI: 10.1134/S0036024421070177/FIGURES/13.

30 S. M. Yakout, A. M. Youssef, M. A. Wahba, W. Sharmoukh, A. M. El Sayed and M. S. Khalil, Superior ferromagnetic and electrical properties: High purity multiferroic $Bi_{0.98}M_{0.02}$-FeO_3 (M = La, Pr, Gd) compositions, *J. Magn. Magn. Mater.*, 2022, **561**, 169751, DOI: 10.1016/j.jmmm.2022.169751.

31 M. A. Wahba, S. M. Yakout, A. M. Youssef, W. Sharmoukh, A. M. E. sayed and M. S. Khalil, Chelating Agents Assisted Rapid Synthesis of High Purity $BiFeO_3$: Remarkable Optical, Electrical, and Magnetic Characteristics, *J. Supercond. Nov. Magn.*, 2022, **35**, 3689–3704, DOI: 10.1007/s10948-022-06425-z.

32 N. A. Lomanova, I. V. Pleshakov, M. P. Volkov, S. G. Yastrebov, K. Kenges, V. L. Ugolkov, A. V. Osipov, T. Siyuan, I. V. Buryanenko and V. G. Semenov, Solution combustion synthesis of $Bi_2Fe_4O_9$ possessing enhanced magnetic and photocatalytic properties, *Inorg. Chem. Commun.*, 2024, **161**, 112109, DOI: 10.1016/J.INOCHE.2024.112109.

33 A. A. Ostroushko, T. Y. Maksimchuk, A. E. Permyakova and O. V. Russkikh, Determinative Factors for the Thermochemical Generation of Electric Charges upon Combustion of Nitrate–Organic Precursors for Materials Based on Lanthanum Manganite and Cerium Dioxide, *Russ. J. Inorg. Chem.*, 2022, **67**, 799–809, DOI: 10.1134/S0036023622060171/FIGURES/6.

34 Z. Shang, T. Wang, A. Ren, Y. Yu, Y. Zheng, Y. Tao, P. Feng, Y. Xiao and X. Wang, Hollow macroporous CeO_2/β-Bi_2O_3 heterostructure sphere via one-step spray solution combustion synthesis for efficient photocatalysis, *Appl. Surf. Sci.*, 2023, **619**, 156718, DOI: 10.1016/J.APSUSC.2023.156718.

35 Z. Shang, Z. Yang, Y. Xiao and X. Wang, Ordered mesoporous Ag/CeO_2 nanocrystalline via silica-templated solution combustion for enhanced photocatalytic performance, *Colloids Surf., A*, 2020, **604**, 125301, DOI: 10.1016/J.COLSURFA.2020.125301.

36 Z. Shang, Y. Yu, H. Yang, Z. Yang, Y. Xiao and X. Wang, One-step solution combustion synthesis of micro-nano-scale porous Cu/CeO_2 with enhanced photocatalytic properties, *J. Rare Earths*, 2023, **41**, 250–258, DOI: 10.1016/J.JRE.2022.02.013.

37 A. A. Ostroushko, I. D. Gagarin, E. V. Kudyukov, T. Y. Zhulanova, A. E. Permyakova and O. V. Russkikh, Synthesis of lanthanum manganite powders via combustion reactions: some aspects of the influence of magnetic field and charge generation in precursors on the formation of properties, *Nanosyst. Physics, Chem. Math.*, 2025, **14**, 571–583, DOI: 10.17586/2220-8054-2023-14-5-571-583.

38 E. A. Tugova, O. N. Karpov and S. G. Yastrebov, Raman scattering features of nanocrystalline neodymium ferrite, *Nano-Struct. Nano-Objects*, 2023, **33**, 100946, DOI: 10.1016/J.NANOSO.2023.100946.

39 J. L. Ortiz-Quiñonez, D. Díaz, I. Zumeta-Dubé, H. Arriola-Santamaría, I. Betancourt, P. Santiago-Jacinto and N. Nava-Etzana, Easy synthesis of high-purity $BiFeO_3$ nanoparticles: New insights derived from the structural, optical, and magnetic characterization, *Inorg. Chem.*, 2013, **52**, 10306–10317, DOI: 10.1021/IC400627C/SUPPL_FILE/IC400627C_SI_002.AVI.

40 V. I. Popkov, M. I. Chebanenko, M. I. Tenevich, I. V. Buryanenko and V. G. Semenov, Solution combustion synthesis of iron-deficient $Sc_{2-x}Fe_xO_3$ (x = 0.17–0.47) nanocrystals with bixbyite structure: The effect of spatial constraints, *Ceram. Int.*, 2022, **48**, 36046–36055, DOI: 10.1016/j.ceramint.2022.08.027.

41 I. V. Buryanenko, V. G. Semenov, N. A. Lomanova, A. V. Osipov, M. P. Volkov and I. V. Pleshakov, Magnetic properties of nanocrystalline material based on $Bi_2Fe_4O_9$, *Phys. Solid State*, 2022, **64**, 539, DOI: 10.21883/PSS.2022.05.53513.274.

42 V. I. Popkov, O. V. Almjasheva, V. N. Nevedomskiy, V. V. Panchuk, V. G. Semenov and V. V. Gusarov, Effect of spatial constraints on the phase evolution of $YFeO_3$-based nanopowders under heat treatment of glycine-nitrate combustion products, *Ceram. Int.*, 2018, **44**, 20906–20912, DOI: 10.1016/j.ceramint.2018.08.097.

43 V. I. Popkov, O. V. Almjasheva, M. P. Schmidt, S. G. Izotova and V. V. Gusarov, Features of nanosized $YFeO_3$ formation

under heat treatment of glycine-nitrate combustion products, *Russ. J. Inorg. Chem.*, 2015, **60**, 1193–1198, DOI: 10.1134/S0036023615100162.

44 K. D. Martinson, I. B. Panteleev, A. P. Shevchik and V. I. Popkov, Effect of the Red/ox ratio on the structure and magnetic behavior of $Li_{0.5}Fe_{2.5}O_4$ nanocrystals synthesized by solution combustion approach, *Lett. Mater.*, 2019, **9**, 475–479, DOI: 10.22226/2410-3535-2019-4-475-479.

45 N. A. Lomanova, M. V. Tomkovich, D. P. Danilovich, A. V. Osipov, V. V. Panchuk, V. G. Semenov, I. V. Pleshakov, M. P. Volkov and V. V. Gusarov, Magnetic Characteristics of Nanocrystalline $BiFeO_3$-Based Materials Prepared by Solution Combustion Synthesis, *Inorg. Mater.*, 2020, **56**, 1271–1277, DOI: 10.1134/S0020168520120110/FIGURES/5.

46 N. A. Lomanova, V. V. Panchuk, V. G. Semenov, I. V. Pleshakov, M. P. Volkov and V. V. Gusarov, Bismuth orthoferrite nanocrystals: magnetic characteristics and size effects, *Ferroelectrics*, 2020, **569**, 240–250, DOI: 10.1080/00150193.2020.1822683.

47 H. Maleki, M. Zakeri and R. Fathi, Experimental study of the effect of yttrium on the structural, thermal, and magnetic properties of $BiFeO_3$, *Appl. Phys. A: Mater. Sci. Process.*, 2018, **124**, 1–6, DOI: 10.1007/S00339-018-2154-8/TABLES/1.

48 N. I. Ilić, J. D. Bobić, B. S. Stojadinović, A. S. Džunuzović, M. M. Vijatović Petrović, Z. D. Dohčević-Mitrović and B. D. Stojanović, Improving of the electrical and magnetic properties of $BiFeO_3$ by doping with yttrium, *Mater. Res. Bull.*, 2016, **77**, 60–69, DOI: 10.1016/J.MATERRESBULL.2016.01.018.

49 Z. A. Samoilenko, N. N. Ivakhnenko, E. I. Pushenko, V. Y. Sycheva, N. A. Ledenev and A. V. Pashchenko, The Influence of the Composition on the Atomic Structure of $Bi_{1-x}Y_xFeO_3$ Ceramics, *Tech. Phys.*, 2021, **66**, 793–797, DOI: 10.1134/S1063784221050212/FIGURES/6.

50 A. Perejón, E. Gil-González, P. E. Sánchez-Jiménez, J. M. Criado and L. A. Pérez-Maqueda, Structural, Optical, and Electrical Characterization of Yttrium-Substituted $BiFeO_3$ Ceramics Prepared by Mechanical Activation, *Inorg. Chem.*, 2015, **54**, 9876–9884, DOI: 10.1021/ACS.INORGCHEM.5B01654.

51 Z. Li, L. Cheng, K. Zhang and Z. Wang, Enhanced photocatalytic performance by Y-doped $BiFeO_3$ particles derived from MOFs precursor based on band gap reduction and oxygen vacancies, *Appl. Organomet. Chem.*, 2021, **35**(3), e6113, DOI: 10.1002/AOC.6113.

52 V. Runco Leal, C. Navarro, G. Bridoux, M. Villafuerte and M. I. Gómez, Preparation and characterization of a new series of solid solutions of $Bi_{1-x}Y_xFeO_3$ $(0 < x < 1)$ from the thermal decomposition of hexacyanoferrates doped with yttrium, *J. Therm. Anal. Calorim.*, 2019, **135**, 3259–3268, DOI: 10.1007/S10973-018-7593-0/FIGURES/11.

53 R. D. Shannon, Revised effective ionic radii and systematic studies of interatomic distances in halides and chalcogenides, *Acta Crystallogr., Sect. A*, 1976, **32**, 751–767, DOI: 10.1107/S0567739476001551.

54 N. S. Parvathy and R. Govindaraj, Atomic scale insights on the growth of $BiFeO_3$ nanoparticles, *Sci. Rep.*, 2022, **12**, 1–17, DOI: 10.1038/S41598-022-08687-Y;SUBJMETA.

55 A. Jakimińska, M. Pawlicki and W. Macyk, Photocatalytic transformation of Rhodamine B to Rhodamine-110 – The mechanism revisited, *J. Photochem. Photobiol., A*, 2022, **433**, 114176, DOI: 10.1016/J.JPHOTOCHEM.2022.114176.

56 I. K. Konstantinou and T. A. Albanis, TiO_2-assisted photocatalytic degradation of azo dyes in aqueous solution: kinetic and mechanistic investigations: A review, *Appl. Catal., B*, 2004, **49**, 1–14, DOI: 10.1016/J.APCATB.2003.11.010.

57 S. M. Tikhanova, M. I. Tenevich, A. N. Matveyeva, M. O. Enikeeva, A. D. Trofimuk, V. N. Nevedomskiy, S. E. Yu, D. S. Dmitriev and V. I. Popkov, Solution combustion synthesis of phase-pure, foam-like hexagonal $LuFeO_3$: visible-light photocatalyst with high activity, *Appl. Surf. Sci.*, 2026, **729**, 166181, DOI: 10.1016/j.apsusc.2026.166181.